Experimental review of wideband OFDM in electronic sub-mmW wireless communication

Simon Haussmann[1] (iD), Florian Euchner[2], Benjamin Schoch[1], Dominik Wrana[1], Axel Tessmann[3] and Ingmar Kallfass[1]

[1]University of Stuttgart, Institute of Robust Power Semiconductor Systems, Stuttgart, Germany; [2]Institute of Telecommunications, University of Stuttgart, Stuttgart, Germany and [3]Fraunhofer Institute for Applied Solid State Physics IAF, Freiburg, Germany

Abstract

In this paper, we demonstrate wideband orthogonal frequency division multiplexing (OFDM) at sub-mmW frequencies with full electronic data and carrier generation. We present the first stringent examination of OFDM-waveform design in a fully electronic experimental setup. Operating at 309 GHz center frequency and modulated channel bandwidths of 2 and 10 GHz, the performance of single-carrier waveforms is compared to OFDM signals with varying modulation formats and subcarrier settings. In addition to the investigation of the gross data rate, which is resulting in 20 Gbit/s for OFDM and 40 Gbit/s for single-carrier, we give one of the first demonstrations of joint communication and sensing with OFDM-signals at sub-mmW frequencies, as the distance between transmitter and receiver isdetermined by examination of the received signal.

Introduction

Orthogonal frequency division multiplexing (OFDM) has revolutionized mobile communication at the beginning of the millennium. In parallel, technologies are currently evolving toward higher carrier frequencies in order to utilize more absolute bandwidths. The mmW-spectrum such as E-, W-, or D-band are currently the focus of on-going research activities for future mobile communication standards, i.e., 6G [1]. Also the H-band (220–325 GHz), located at the brink between the mmW and the sub-mmW domain, is envisioned to play a crucial role in future communication and sensing applications. In these, also referred to as THz or sub-THz bands, at first only single-carrier (SC) modulation schemes have been pursued due to their robustness and easy implementation. In emerging standards, like the IEEE802.15.3d [2], although multiple sub-bands can be assigned with different channel-identifiers, only SC modulation is considered, leaving room for classical FDM. OFDM has not yet been included. However, with massive MIMO or joint communication and sensing (JCAS), more sophisticated waveforms like OFDM find their way into experimental setups and demonstrators. Especially for channel sounding, with its comparable lower equalization complexity, OFDM can bring many advantages in future sub-mmW communication or sensing applications. This leads to additional waveform design choices, like the preamble-, pilot-, or subcarrier-design. Up to the authors knowledge, the choice of these parameters has not yet been discussed based on empirical data for the distinct conditions present at THz frequencies in comparable studies.

The goal of this paper is to comprehensively compare the performance of SC communication and OFDM and thus to evaluate the feasibility of OFDM at sub-mmW communication in a fully electronic setup. A special focus lies on system impairments and their influence on waveform design choices. Like in most wireless communication scenarios, the carrier-signals of the transmitter and receiver are generated independently, so no phase-coherent coupling is present. Further, we want to give insights on OFDM waveform design and its impact on the signal quality at THz.

Section "OFDM at mmW and sub-mmW" introduces the state of the art and compares waveform design of both, SC and OFDM waveforms. Following section describes a wireless communication experiment, designed to investigate OFDM-waveform design choices in a 300-GHz communication link. In the experiment, the introduced SC and OFDM waveforms from Section "OFDM at mmW and sub-mmW" are applied to the wireless system. In the following section, the results are discussed in terms of signal quality and potential sensing capabilities based on the equalizers channel response are introduced.

CAMBRIDGE UNIVERSITY PRESS

OFDM at mmW and sub-mmW

In recent years, many communication experiments centered around 300 GHz have been reported, showcasing the feasibility of primarily point-to-point communications links. Most of them are academic studies with a wide variety of techniques and technologies. Table 1 shows an overview of recent reported wireless communication experiments at mmW- and sub-mmW frequencies [3–13]. Optical as well as electronic and hybrid technologies are used. It is listed, whether a SC waveform, an FDM-approach or an ODFM waveform has been used to achieve the data rate. Communication range, antenna system, spectral efficiency and polarization configuration are not included in this survey, which prohibits a direct comparison of all publications. We want to highlight [3], which reports very high data transfer rates (DTR) of over 200 Gbit/s at W-band with optical modulation, time-frequency equalization techniques, probabilistic shaping and utilization of 30 GHz of bandwidth. With [4], also a SiGe-based fully electronic communication system, reaching 100 Gbit/s over 60 cm distance,

is presented. OFDM mostly plays a role in mmW-systems in E-band and in D-band but above 200 GHz center frequency, SC is mostly reported. The highest data rates are not achieved by a high spectral efficiency, but rather by large channel bandwidths and SC modulations. [8] and [12] are using SC-modulations with multiple tens GHz of bandwidth with optical mixing to generate gross-data rates over 200 Gbit/s. Although OFDM at THz frequencies is mostly employed in photonic systems (i.e., [13]), with [6] also fully electronic OFDM-demonstrations are documented. Recent FDM-approaches are reported as well [5], [10]. These experiments achieve lower data rates, but demonstrate outdoor, real-time and long-term installations. Multiple modems- or real-time channels are aggregated to increase the data rate of the link. The listed publications present either a single waveform configuration or a restricted selection of modulation formats. In order to give valuable experiment-based insights for waveform design techniques, we present in our work a comprehensive waveform study along with a JCAS implementation example in a wireless link. In order to classify the influence of different system impairments on the signals, our measurements are conducted with a high system margin, resulting in lower datarates compared to the state of the art.

Table 1. Recently reported wireless communication experiments at mmW and sub-mmW frequencies

Ref. year	f_c GHz	DTR Gbit/s	Technology	Modulation	Add. Funct.[a]
[3] 2021	92.5	**204.8** simplex	phot.	OFDM[b] PS-QAM	
[4] 2022	220	100 simplex	**SiGe**	SC 16QAM	BIST[c]
[5] 2024	220	83.2 simplex	electronic	FDM 16QAM	Real-time 8K-Video
[6] 2024	220	20.8 **duplex**	GaAs & InP	OFDM 16QAM	
[7] 2014	240	96 simplex	InGaAs	SC 8PSK	
[8] 2024	275	**220** simplex	phot.	SC 32QAM	
[9] 2020	290	120 simplex	InP	SC 16QAM	
[10] 2024	295	20 **duplex**	phot.& InGaAs	FDM 32QAM	**IP data traffic[d]**
[11] 2020	300	96 simplex	InGaAs	SC 16QAM	
[12] 2023	300	200 simplex	phot.	SC 16QAM	
[13] 2017	305	40 simplex	phot.	OFDM on-off[e]	
This work	**309**	32 simplex	InGaAs	SC 16QAM	
This work	**309**	20 simplex	InGaAs	OFDM QSPK	**JCAS & waveform study[f]**

[a]Additional functionalities.
[b]Probabilistic shaping (PS) with 128-QAM and 512-QAM OFDM-modulations.
[c]Implementation with build-in-self-test (BIST).
[d]Data-rate reflects real-time network integrated data-traffic.
[e]Modulation scheme is on-off-keying.
[f]For the first time an example for JCAS at mmW-frequencies is given and a variety of waveform design-parameters is investigated with focus on electronic THz-impairments.

Single-carrier waveforms

The SC waveform generation in THz communication in most publications uses quadrature amplitude modulation (QAM) or phase shift keying (PSK)-modulated waveforms, applied to an analog carrier, either homodyne or heterodyne. To enhance spectral efficiency and to decrease adjacent channel leakage, the modulated waveform is pulse-shaped with a root-raised cosine filter (RRC) in the transmitter and with a matched filter in the receiver. The signal bandwidth is equal to the symbol rate multiplied by 1 plus roll-off, as indicated by Fig. 1(a). Additionally, the RRC filtering is increasing the peak-to-average-power-ratio (PAPR) of the waveform as compared to rectangularly filtered symbols. Throughout this work, a roll-off of 0.25 is applied. In conjunction with symbol rates of 1.6 and 8 GBd this leads to channel bandwidths of 2 and 10 GHz. In the demodulator digital carrier and symbol-timing recovery algorithms are used to demodulate the signal.

OFDM waveforms

OFDM is just recently emerging for mmW-frequency bands. Suffering mostly from high PAPR with almost no high bandwidth linearization techniques available, OFDM has the disadvantage of a reduced link budget in comparison to SC waveforms. Also, high phase noise (PN), especially in electronic systems lead to inter-carrier-interference impeding multi-carrier approaches. There is currently much progress in OFDM waveform and system design techniques that are targeting these issues. According to [14] discrete Fourier transform (DFT)-spread OFDM can reduce the PAPR of OFDM signals by 3 dB and reduce the influence of Doppler spread. Also, sub-band spreading can be a viable option for targeting channel interference for multiple data streams [15]. Convolutional networks and deep-learning are able to enhance OFDM-system design. i.e. for accelerated and more efficient receiver processing [16], can make efficient pilot [17] or modulation design [18].

To maintain comparability and to allow a universally applicable outcome of this work, an OFDM implementation, adapted from the 802.11a standard [19] is used in our experiments. In order to give a guideline on waveform design, especially subcarrier spacing
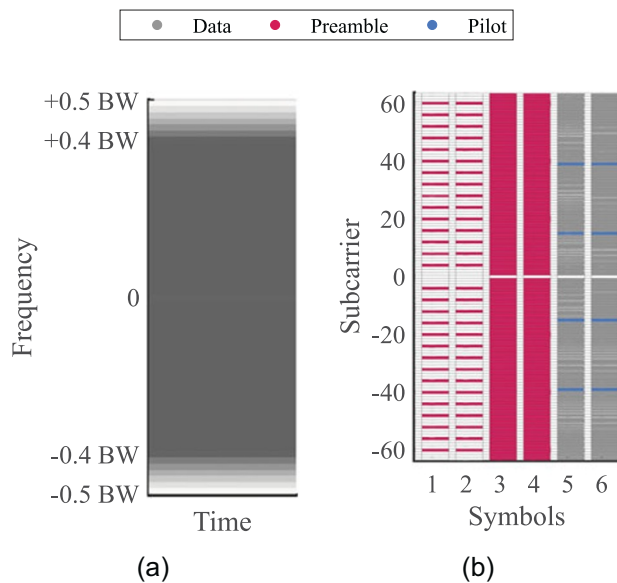
Figure 1. Waveform design for OTA-experiments. (a) Time-and frequency domain of the used SC-waveforms with a roll-off factor of 0.25. (b) Exemplarily the applied OFDM symbol map for FFT of size 128.

at sub-mmW, experiments with different number of subcarriers and experiments with 2 and 10 GHz bandwidth are carried out. To use as much bandwidth as possible, the number of upper guard bands is zero. Just one lower guard band is inserted to maintain symmetry of the spectrum. Also, the center subcarrier is in idle state constantly. This results in ($N_{FFT} - 2$) active subcarriers with N_{FFT} being the size of the applied fast Fourier transform (FFT). According to 802.11a the OFDM frame starts with a two-stage training sequence, each consisting of two preambles symbols: Two symbols with reduced number of active subcarriers, followed by two preambles where all active subcarriers are used to train the equalizer. Finally, data-symbols are following, whereas four pilot carriers are maintaining phase consistency. The training sequence and the pilot signals are BPSK-encoded.

The first training segment has a reduced number of active subcarriers by factor of four, therefore a higher amplitude ($a_{Sym.1,2}$) is chosen for this segment in relation to the rest of the OFDM symbols to maintain an equally high envelope power over the OFDM symbol:

$$a_{Sym.1,2} = \sqrt{\frac{N_{active}}{N_{Sym.1,2}}} = \sqrt{\frac{N_{FFT} - 2}{N_{FFT}/4 - 2}}. \quad (1)$$

Figure 1(b) shows the OFDM symbol map for an FFT-size of 128. Other FFT sizes had been generated similarly with a two-stage training sequence and four pilot tones distributed over the data field. Experiments show that in the system and the channel impulse response (IR), refer to Fig. 9, no major contribution after 10 ns is present, which enables guard intervals (or cyclic prefixes, respectively) to be a fraction of the symbol duration. With symbol durations of 16, 32, 64, and 128 ns for 32-FFT, 64-FFT, 128-FFT, and 256-FFT, respectively, and 2 GHz bandwidth, the corresponding fraction of guard-interval to symbol duration equals to 38%, 24%, 14%, and 7%. These guard intervals are also accounted for in the calculation of the spectral efficiency in Fig. 2.

Waveform comparison

Recent publications are already discussing the applicability of OFDM at sub-mmW frequencies and conduct a performance comparison to SC modulations [20–23]. In the publications, hardware impairments like PN and amplifier compression are evaluated, modelled and applied to broadband simulations, but a comparable study of actual broadband measurements is not yet presented.

Figure 2 shows a comparison between the waveforms we considered in this paper in terms of spectral efficiency and PAPR, defined as the ratio between the maximum signal power and the RMS signal power in the digital base band (BB). SC has the lowest PAPR, which is largely dependent on the modulation format and the RRC-roll-off factor. In OFDM, the PAPR is generally higher, but the difference of the PAPR, which varies between 9 and 13 dB increases only slightly over the number of subcarriers. The graph shows also the spectral efficiency for the chosen waveforms: For SC it is equal to the spectral efficiency of the modulation format multiplied by 0.8 due to the roll-off. For OFDM, the share of pilots is decreasing the spectral efficiency, which affects modulations with a lower number of subcarriers more. Additionally, the cyclic prefix, discussed in the previous section is taken into consideration as well. In the regarded case for 2 GHz bandwidth and an IR duration of 10 ns, the spectral efficiency of OFDM gets higher than SC for FFT-sizes larger than 64. This applies under ideal conditions. In the next step, the waveforms from Fig. 2 are tested under sub-mmW conditions.

Wireless communication experiment

In order to validate the applicability of OFDM in the sub-mmW domain, over-the-air (OTA) experiments under laboratory conditions are carried out. Figure 3 shows the block diagram of the measurement setup. The system has a superheterodyne architecture and is mostly based on electronic semiconductor components in a 35-nm InGaAs mHEMT technology [24].

Full electronic sub-mmw experimental setup

As the system architecture is superheterodyne, the setup consists of an IF-up-conversion stage bringing the signal to a center
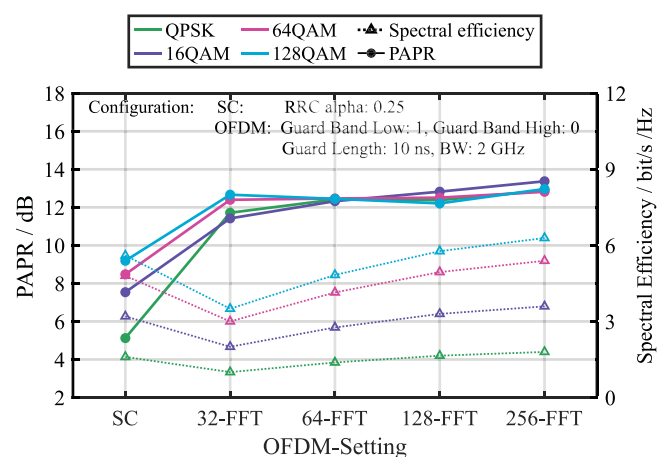

Figure 2. Comparison of PAPR and spectral efficiency between different waveform configurations.
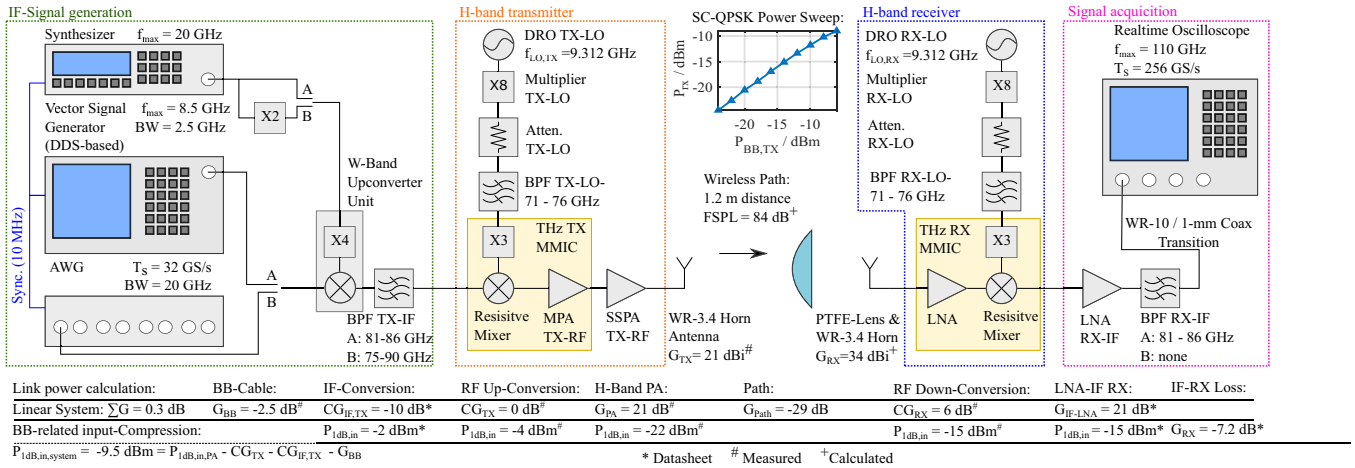
Figure 3. Block diagram of OFDM OTA measurement setup. Configuration A is for 2 GHz channel BW, while configuration B yields 10 GHz BW.

Link power calculation:	BB-Cable:	IF-Conversion:	RF Up-Conversion:	H-Band PA:	Path:	RF Down-Conversion:	LNA-IF RX:	IF-RX Loss:
Linear System: $\sum G = 0.3$ dB	G_{BB} = -2.5 dB[#]	$CG_{IF,TX}$ = -10 dB*	CG_{TX} = 0 dB[#]	G_{PA} = 21 dB[#]	G_{Path} = -29 dB	CG_{RX} = 6 dB[#]	G_{IF-LNA} = 21 dB*	
BB-related input-Compression:		$P_{1dB,in}$ = -2 dBm*	$P_{1dB,in}$ = -4 dBm[#]	$P_{1dB,in}$ = -22 dBm[#]		$P_{1dB,in}$ = -15 dBm[#]	$P_{1dB,in}$ = -15 dBm*	G_{RX} = -7.2 dB*

$P_{1dB,in,system} = -9.5$ dBm $= P_{1dB,in,PA} - CG_{TX} - CG_{IF,TX} - G_{BB}$ * Datasheet   [#] Measured   [+]Calculated

of 83.5–85.5 GHz followed by the superheterodyne H-band up-conversion mixer (reported in [25]) and a power amplifier (PA) [26]. The wireless path consists of a corrugated horn antenna at the TX and a Teflon lens in conjunction with a horn antenna at the RX. The additional gain of the lens-horn combination is estimated by comparing the aperture of the horn antenna with the illuminated area on the lens:

$$G = G_{horn} + 20 \cdot \log_{10}\left(\frac{2 \cdot \tan(\phi \cdot 0.5) \cdot l_{foc}}{d_{horn}}\right), \quad (2)$$

with the gain of the horn G_{horn} being 21 dBi, the opening angle (half-power beam-width) of the horn ϕ of 12°, the focal length of the lens l_{foc} = 151 mm and d_{horn}, the diameter of the horn aperture, 7 mm. This results in a gain of 34 dBi, which has been verified by measurements. The wireless path covers a range of 1.2 m. Absorbers are used to prevent multipath effects. At the receiver a down-conversion mixer translates the signal back to IF, where it is sampled directly by a real-time sampling oscilloscope. An additional LNA at the RX IF-interface amplifies the signal level to improve the acquired signal quality. The signal evaluation is done offline. The local oscillator (LO) for the H-band frontends is generated electronically using dielectric resonator oscillators (DRO) and frequency multiplication stages. One multiplication stage by eight converts the tone to E-band, from 9.312 to 74.5 GHz. A frequency tripler, which is directly integrated on the frontend MMICs, converts the oscillator tone to 223.5 GHz. It is noted, that both are free-running DROs, so both frontends are incoherent. Also, only the frequency generation laboratory equipment is synced by a 10 MHz signal, the real-time oscilloscope is using its internal independent frequency reference.

Figure 4 highlights the performance of some key elements of the experiment. Figure 4(a) shows the conversion gain (CG) of the TX and RX range over the IF frequency, when operated with 3 dB LO power. The TX has an average of 0 dB CG over the frequency with an output related 1 dB compression point at - 4 dBm. The RX has 6 dB CG and a $P_{1dB,out}$ of -15 dBm in the targeted frequency range. Figure 4(b) shows a VNA measurement of the PA compression in terms of AM-AM and AM-PM relations. The gain partitioning of the experiment ensures, that the PA is the first component driven into compression so the PA is mainly influencing the non-linearities in the link. The measured single-sideband PN of the DROs, which are used as LO-oscillator source can be seen in Fig. 4(c). The PN of the fundamental tone is shown as well
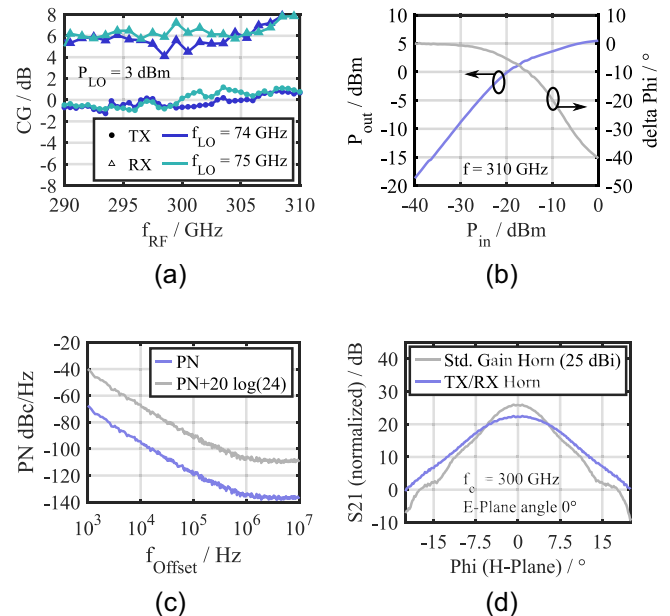

Figure 4. Performance of the key components of the measurement setup. (a) Conversion gain of the TX and RX modules for H-band conversion. (b) VNA bases AM-AM and AM-PN of the SSPA. (c) Measured single sideband PN of the DROs with estimated contribution of multiplication stages. (d) Antenna pattern of the horn antenna in relation to a standard-gain horn.

as an estimation of the PN after the multiplication stages, which enhances the PN ideally according to $20 \cdot \log_{10}(N)$ with N being 24. Finally, the measured antenna patterns are displayed in Fig. 4(d) resulting in 21 dBi of antenna gain and an HPBW of 12°.

In order to address the two individual channel configurations of 2 and 10 GHz channel bandwidth, different setup-choices are explained in the following sections:

2-GHz bandwidth experiments

In case of the 2-GHz channel assignment, the modulated waveform (SC or ODFM) is generated by a direct digital synthesis (DDS)-based vector signal generator. A digital carrier-frequency of 5.5 GHz is applied. An analog synthesizer generates a tone of
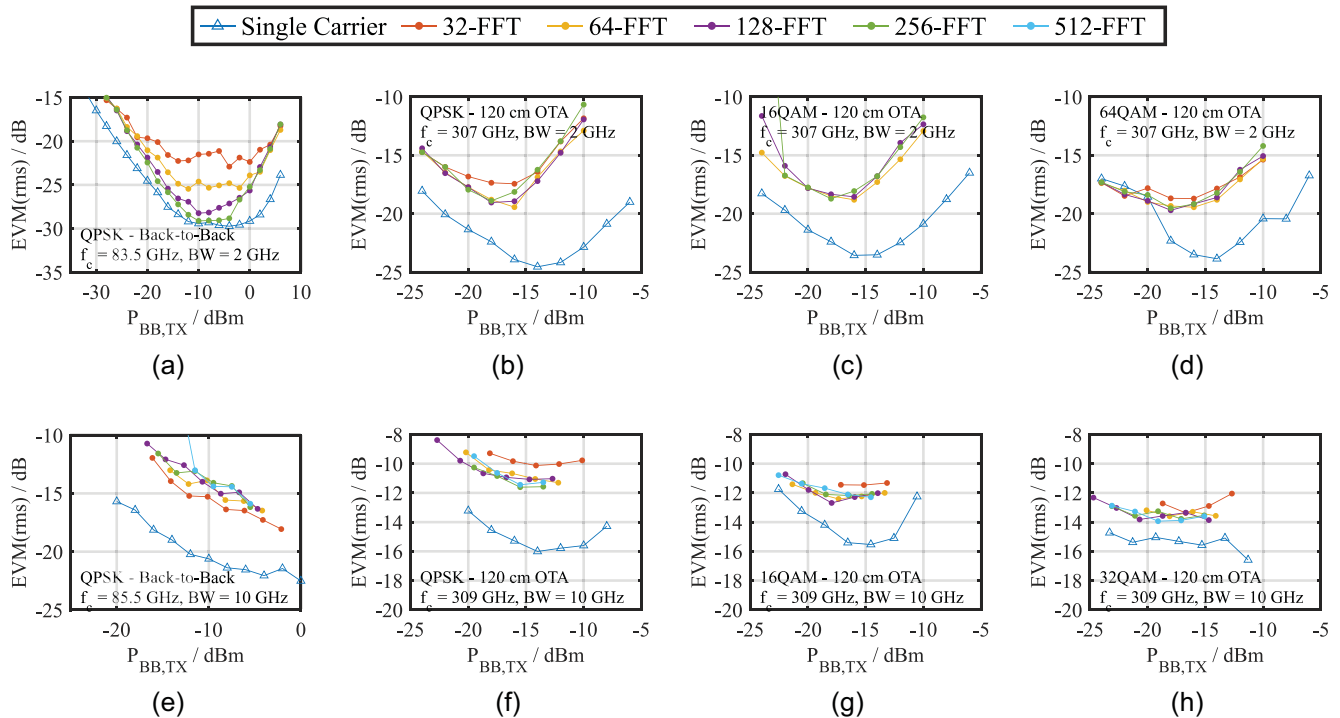
Figure 5. EVM performance of wideband OFDM compared to SC scenario. (a) and (e) Back-to-back characterization of the IF-system. (b)–(d) Sub-mmW OTA performance with 2 GHz channel bandwidth. (f)–(h) Performance of 10 GHz bandwidth, respectively.

19.5 GHz. In the W-band upconverter unit, this adds up to a new center frequency of the broadband signal of 83.5 GHz. The filter BPF TX-IF is filtering the lower sideband as well as all LO leakage and harmonics from the carrier generation. The additional 223.5 GHz LO-tone in the H-band mixer results in a new center frequency of 307 GHz, which is transmitted over the air. The spacing between RF-signal and oscillator leakage is 83.5 GHz which avoids interference between LO leakage and RF-signal due to the superheterodyne concept. At the receiver's IF interface the BPF RX-IF is filtering out remaining LO leakage from the down-conversion stage.

10-GHz bandwidth experiments

In case of the 10-GHz channel setting, an arbitrary waveform generator (AWG) is used to modulate the data, as the vector signal generator provides only an instantaneous bandwidth of 2.5 GHz. Thus, the spectral purity and the higher dynamic range can not be used anymore. A digital offset frequency of 8 GHz is applied in the digital domain. Mixed with a 11.69 GHz fundamental tone, which is first doubled and then applied to the same up-conversion unit with integrated frequency quadrupler, an LO-frequency of 93.5 GHz is applied to the broadband signal, which centers the lower sideband of the broadband signal at 85.5 GHz. A 90 GHz WR-10 waveguide low-pass filter blocks the upper mixer image and the LO-leakage from entering the H-band stage. At the receiver side, no additional filtering is applied between the analog frontend and the oscilloscope.

Back-to-back characterization

To validate the measurement setup, a first back-to-back characterization is carried out, which verifies that the H-band channel

and hardware and not the measurement environment is limiting the quality of the link. In the back-to-back configuration, the IF-interface is directly connected to the sampling oscilloscope which is synced by a 10 MHz clock with the signal generation. In the error vector magnitude (EVM)-plots in Fig. 5(a) and 5(e), the resulting signal quality is displayed. The EVM is defined by equation (3) and (4). The root mean square (RMS) amplitude of the non-data-aided error vector e of a subcarrier n in relation to the RMS amplitude of the reference constellation, which is normalized to 1, gives the EVM of a single subcarrier. The number of considered symbols M is chosen to be 1000 for SC and 60 for OFDM. In the OFDM experiments, the EVM of all data-subcarriers N_{data} is averaged with RMS as well, whereas the EVM of the pilots and preambles are not taken into consideration. For SC, N_{data} is equal to 1.

$$\text{evm} = \sqrt{\frac{1}{N_{\text{data}} \cdot M} \sum_{n=1}^{N_{\text{data}}} \sum_{m=1}^{M} e_n[m]^2}, \qquad (3)$$

$$\text{EVM} = 20 \cdot \log_{10}\Big(\text{evm}\Big). \qquad (4)$$

In the EVM plot three regions are visible: The noise-defined region up to -12 dBm of input power, then a region with constant EVM until the EVM is degraded by the compression of the IF upconverter. The noise-defined region is a superposition of the thermal noise and the quantization noise, originating from the oscilloscope range, which has a minimum setting of 60 mV full-scale (-17.5 dB peak-power). It is observed, that OFDM signals have between 2 and 3 dB higher EVM in the noise defined region. The authors assume this is due to slight non-linearities in the active components, which is elaborated in more detail in section "Communication Evaluation". Additionally higher EVM at the outer subcarriers spoil the averaged EVM. In the constant EVM region OFDM and SC

waveforms are performing equally, provided that the subcarrier spacing ensures frequency-flat sub-channels. For OFDM signals an earlier compression can be observed due to the higher PAPR. For 10 GHz bandwidth, the experiments are mostly noise-defined, Fig. 5(e). Due to a different signal generation, less BB power is available.

Assessment of link-quality

As a first step of measurement validation, before evaluating link quality in terms of communication and sensing capabilities, the measured power levels are validated using the individual component performances. The linear system amplification, considering the transmitter, path and receiver is estimated to be $+0.3$ dB, as indicated in the lower part of Fig. 3. First saturation of the PA theoretically occurs at -9.5 dBm of BB input power. The measured system amplification from signal generator output to the oscilloscopes input is measured to be -0.6 dB, which lies within the expected precision. The additional attenuation is presumed to result either from additional losses, especially in the WR-3.4 waveguide transitions, dielectric loss in the lens or through reflections or refractions in the wireless path. The power measurement can be observed in the center of the block diagram in Fig. 3, which shows also the expected PA saturation. To provide reproduceable measurements and to avoid dependencies of the equalization quality to the digital recovery of the signal in presence of noise, the equalizer of the SC-experiments is extracted in the optimum operation point using QPSK. However, the OFDM experiments are carried out without a fixed equalization, so the equalizer response is extracted during runtime.

Communication evaluation

The results of the link experiments can be observed in Fig. 5. Opposed to the back-to-back measurement, while varying the signal power, a direct transition from noise-defined to compression-defined is observed.

The authors assume, that OFDM only can be operated within limits in sub-mmW systems: As the channel and the frontend components do not have a flat frequency response, also seen in Fig. 8, an upper limit of channel spacing is required to ensure frequency-flat subchannels. On the other hand, PN induces inter-carrier-interference leading to a lower-limit of subcarrier spacing. As almost no influence on the signal quality is observed between the subcarrier settings, inter-carrier-interference resulting from PN is assumed to be low. However, for 32 subcarriers and 2 GHz BW, resulting in 62.5 MHz of subcarrier spacing, the EVM is measurably higher, probably due to non-flat subchannels. So generally, for fully electronic OFDM-systems, a subcarrier spacing of less or equal to 31 MHz is advised based on the obtained empirical data. The lower limit, defined by the PN could not be identified. The memory of the used measurement equipment needs to replay or capture the duration of multiple symbol duration which is inversely proportional to the subcarrier spacing. This restricts experiments with 1024-FFT or higher. However, this restriction may apply to most system implementations, making it unlikely to exceed 512-FFT.

The 10-GHz results show significantly higher EVM. As the BW is five times higher we expect a 7 dB decrease in SNR and additionally higher amplitude and group delay ripple in the channel. So, the observed signal quality is in the range of expectations when compared to the 2-GHz results. Like in the back-to-back measurements, the higher PAPR of OFDM is leading to earlier compression
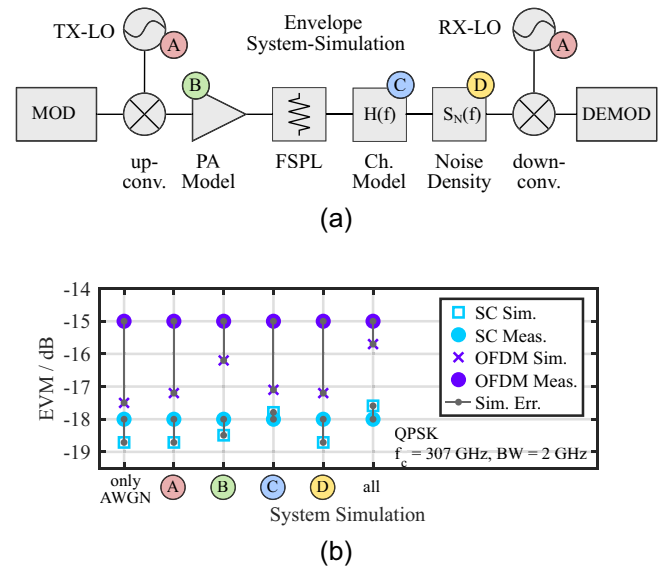

Figure 6. System simulations that are used to classify the influence of selected system impairments on the signal quality. (a) Block diagram of the simulation. (b) Simulation results for 2-GHz QPSK along with a comparison to the obtained measurement data..

or a higher required back-off. Also, as seen in the back-to back measurement, OFDM has a general 4 dB SNR penalty in the noise-defined measurement points. To identify the origin of the differences, we conducted system-level simulations based on abstracted behavioral models based on the used hardware. The simulation setup is implemented according to Fig. 6(a) and different impairments are successively inserted to see the effect on the signal. The same modulation and demodulation techniques as in the measurement are applied. The results are compared to the actual measurement. Exemplarily the 2-GHz-BW QPSK measurement with -24 dBm input power is analyzed. Option A, represents the PN in the LO generation, option B activates the non-linearities in the PA model, C inserts a channel model, which has been extracted from the measurement. Finally, option D alters the simulated noise density to a non-white noise distribution, with a variation of 5 dB over the channel, whereas the total noise power remains equal. The results are shown in Fig 6(b). Although the operation point has the highest back-off from PA compression, the non-linearities have the most influence on the OFDM signal. This is due to the high PAPR in conjunction with a soft transition into PA compression. Whereas the non-flat channel has most influence on the demodulation of the SC signal. PN and non-white noise distribution have low influence on the signal quality. For visualizing the lower EVM of SC modulation, Fig. 7 is showing constellation diagrams for selected waveform configurations in the optimal power setting for SC and OFDM for both channel settings as measured in the OTA link.

As the achieved data-rate is significantly influenced by the Forward-Error-Correction (FEC) algorithm, we want to exclude the FEC-performance from our study to maintain comparability. Exemplarily, the FEC-limit of a state-of-the-art FEC publication is applied to obtain realistic data rates. [27] reports a multi-Gbit staircase decoder, which achieves a BER of 10^{-15} for a pre-FEC-BER of $1.82 \cdot 10^{-2}$ with an overhead of 25%. This pre-FEC-BER is applied to the measurement results:

Ref [28] gives a relation between EVM and an equivalent BER. This calculation assumes AWGN as sole impairment which
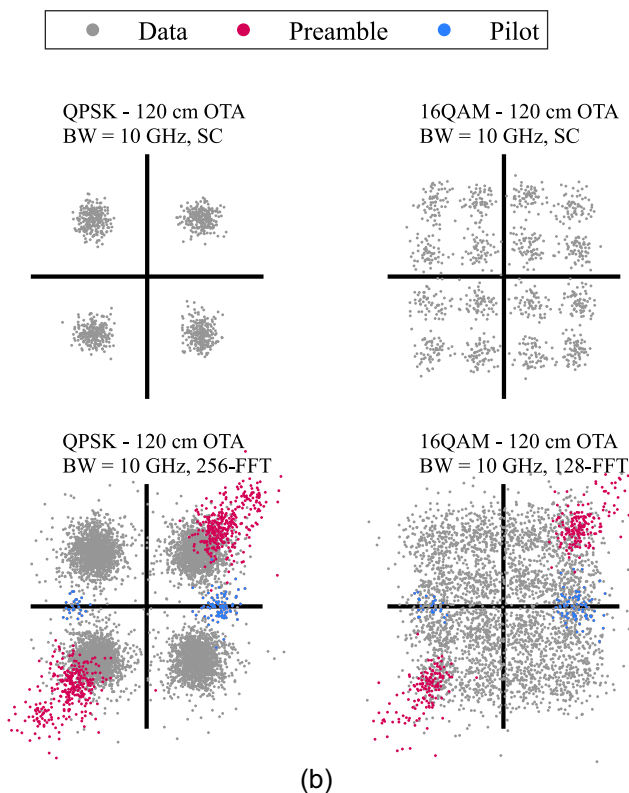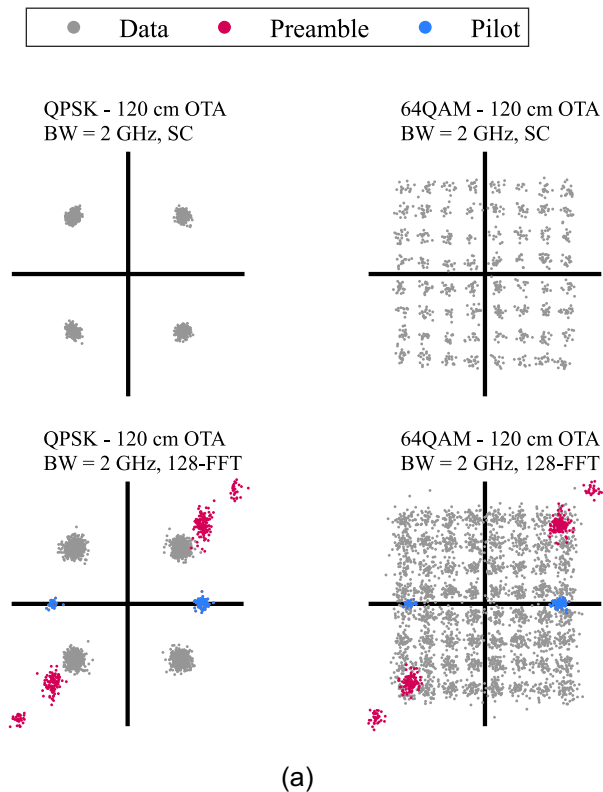
Figure 7. Constellation diagrams for selected system configurations. (a) Measurements with 2 GHz channel bandwidth. (b) Results for 10 GHz channel bandwidth.
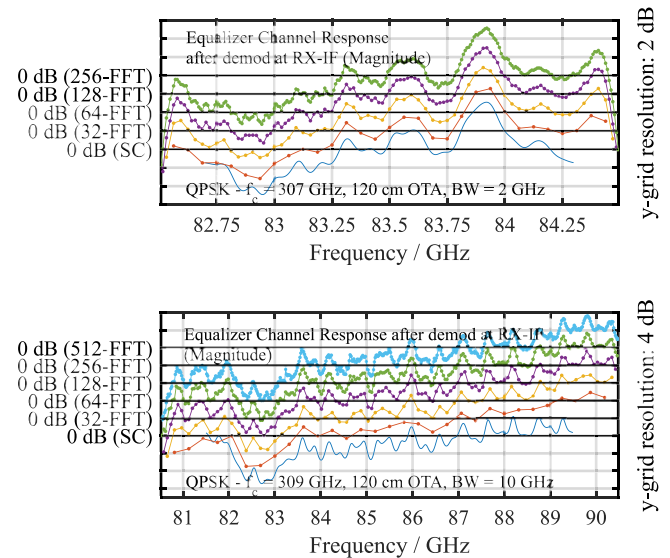

Figure 8. Comparison of equalized channel responses for different bandwidths and subcarriers spacing. The 0 dB-reference of the different channel responses are shifted along the *y*-axis to achieve better visibility.
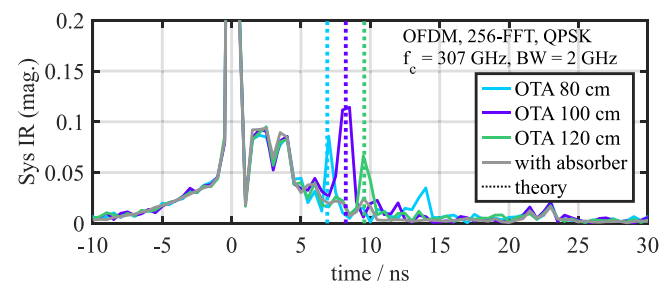

Figure 9. IFFT of the equalized channel response gives the systems impulse response (IR). The IR can be used to sense the distance between TX and RX.

introduces some inaccuracies but holds true the noise-defined region. To ensure proper decoding we assume $1.82 \cdot 10^{-2}$ for the FEC limit, which results in maximum allowable EVM of:

- QPSK – EVM-limit -7.5 dB
- 16QAM – EVM-limit -15.0 dB
- 32QAM – EVM-limit -18.1 dB
- 64QAM – EVM-limit -21.4 dB

Consequently, this limit is still met for 64QAM (SC, 2 GHz), for 32QAM (OFDM, 2 GHz), for 16QAM (SC, 10 GHz) and for QPSK (OFDM, 10 GHz). This corresponds to a maximum achieved pre-FEC-data rate of 32 Gbit/s with SC-modulation and 20 Gbit/s with OFDM in this experiment. The authors want to emphasize, that with additional signal processing techniques, like the Waterfilling-Algorithm (i.e. [29]) the data rate of the OFDM-link can be further improved.

Sensing evaluation

Radio sensing (i.e. defined between 6.49 and 9.95 GHz by [30]) is an existential part of mobile radio technology. The scenario we

target, is foremost a communication link, where additional information about the path or obstacles should be extracted, whilst the data transmission is not interrupted. For validation of these sensing capabilities in the sub-mmW-domain, information from the equalizer is analyzed in order to extract physical characteristics of the channel. The setup from Fig. 3, which is a static link, is used, so only information of location and not information of velocity is evaluated. Figure 8 shows the magnitude of the equalizers for QPSK with a BB power of -16 dBm for both BW settings. For 2 GHz BW the equalized channel response has amplitude deviations of approximately 10 dB, for 10 GHz BW it is 19 dB. It can be clearly seen, that for 32 subcarriers the flat-channel assumption is not valid as the fluctuations of the channel are not captured.

To induce multipath effects, the absorbers in the measurement setups are removed and the link distance is varied in three steps: 120, 100, and 80 cm. The link is operated with 2 GHz bandwidth, OFDM with an FFT-size of 256 and QPSK modulation format. An IFFT of the acquired frequency-domain equalized channel response gives the systems time-domain impulse response (IR). The amplitude of the IR can be seen in Fig. 9. A clear time-delayed multipath contribution can be observed, which is further used to evaluate the distance in the laboratory. Time-delayed reflections can be observed at 7, 8.5, and 9.5 ns for the different distances. The authors assume the multipath results from multiple reflections on the surface of the front-end modules, which are manufactured in gold-plated brass. Another multipath is unlikely, because of the directivity of the lens-horn combination at the RX. Further the multipath has been verified with added absorber material. Fig. 10(a) shows the laboratory setup along with a sketch explaining

the occurring multipath, the geometries and the definition of the distances in Fig. 10(b). The line-of-sight (LOS) path length from the aperture of the RX horn to the aperture of the TX horn is equal to the distance d added to the focal length of the dielectric lens l_{foc} (151 mm) minus the distance from the aperture to the phase center $l_{\text{A,PC}}$, which is 7.6 mm. Additionally the PTFE lens with ϵ_r of 2 and a thickness d_{lens} of 30 mm has a slower phase velocity. In total this leads to a total time delay of the LOS $t_{\text{d,LOS}}$ of:

$$t_{\text{d,LOS}} = \frac{d + l_{\text{foc}} - l_{\text{A,PC}}}{c} + \frac{d_{\text{lens}} \cdot \sqrt{\epsilon_{\text{r,PTFE}}}}{c}, \qquad (5)$$

with d being the link distance, c being the speed of light. The time delay of the multipath is equal to

$$t_{\text{d,MP}} = 3 \cdot t_{\text{d,LOS}} + 4 \cdot \frac{l_{\text{horn}}}{c}, \qquad (6)$$

with the length of the horn l_{horn} of 24 mm. This results in a time delay between LOS and the multipath of

$$\Delta t_{\text{d}} = t_{\text{d,MP}} - t_{\text{d,LOS}} = 2 \cdot t_{\text{d,LOS}} + 4 \cdot \frac{l_{\text{horn}}}{c}, \qquad (7)$$

This leads to a theoretical time delay of 6.90, 8.23, and 9.57 ns for the individual distances.

As Fig. 9 shows, this time delay is visible in the equalizer's IR. The observed time delays for the different distances agree with the theoretical value from equation (7). As additional curve in the plot, the IR of the link with absorber material is included as well, showing that the multipath is suppressed completely. The timesteps are inversely proportional to the bandwidth, which results in 0.5 ns,
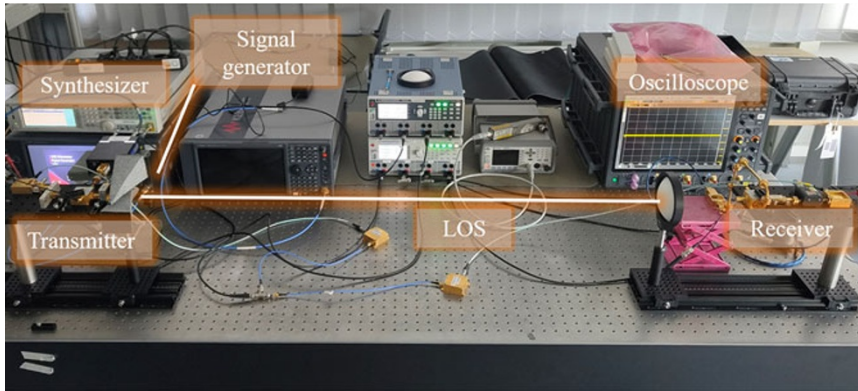
(a)
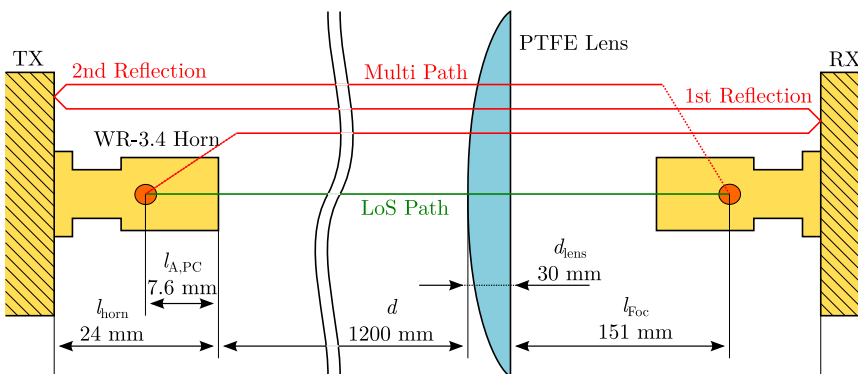
(b)

Figure 10. Sketch of the occurring multipath. (a) Picture of the laboratory setup. (b) Sketch of the multipath for distance estimation..

which defines the granularity of the response. An error propagation analysis gives the accuracy of the sensing: Eq. (5) is inserted in (7) and solved for *d*. *C* stands for the sum of all constant lengths resulting from converting the equations. Differentiation of the formula and multiplying with half of the IFFT-timesteps as Δt_d in the equation gives the minimal accuracy of the distance-sensing, Eq. (9).

$$d(\Delta t_d) = 0.5 \cdot \Delta t_d \cdot c - C, \tag{8}$$

$$d_{\text{error}} = d(\Delta t_d)' \cdot \Delta t_d = 0.5 \cdot c \cdot \Delta t_d. \tag{9}$$

In conclusion, the link distance is estimated by the equalizer information with an accuracy of 3.75 cm for 256-OFDM, which is verified by measurement. As discussed in [31], bistatic OFDM-radars offer a sensing accuracy of *c* divided by the bandwidth wich results in 3.75 cm in our case, which is in line with our results. With advanced processing techniques like super-resolution (i.e., [32]) the sensing quality is potentially improvable. Based on OFDM Doppler-shift estimation, the sensing is extendable towards relative velocities.

Conclusion

In this paper we conduct an experimental comprehensive study on the impact of OFDM waveform design choices on a sub-mmW communication link while demonstrating one of the highest carrier frequencies in a fully electronic OFDM setup. According to our measurements SC signals yield generally lower EVM than OFDM. We conclude nevertheless, that OFDM offers robust performance in terms of synchronization and equalization and can play a viable role in sub-mmW communication. Thus, OFDM should be part of future standardization in addition to the currently considered SC waveforms. Further, we give one of the first documented examples for joint communication and sensing in this frequency domain, achieving a gross-data rate of 20 Gbit/s while being able to sense the distance between transmitter and receiver with an accuracy of 3.75 cm.

References

1. **Eichler T and Ziegler R** (2022) *White paper: Fundamentals of THz Technology for 6G*. Munich, Germany: Rohde und Schwarz.
2. **IEEE** (2024) *IEEE Standard for Wireless Multimedia Networks*. pp. 1–684.
3. **Wang K, Zhao L and Yu J** (2021) 200 Gbit/s photonics-aided MMW PS-OFDM signals transmission at W-Band enabled by hybrid time-frequency domain equalization. *Journal of Lightwave Technology* **39**, 3137–3144.
4. **Grzyb J, Rodríguez-Vázquez P, Malz S, Andree M and Pfeiffer UR** (2022) A SiGe HBT 215–240 GHz DCA IQ TX/RX Chipset with built-in test of USB/LSB rf asymmetry for 100+ gb/s data rates. *IEEE Transactions on Microwave Theory and Techniques* **70**, 1696–1714.
5. **Cao H, Wang Z, Wang W, Zhang Z, Li W, Zhou T, Zhou H, Dong Y, Wang H, Yang Q, Wang X, Xu Q, Yang Z, Zeng H, Huang L and Zhang Y**

6. **Zhou T, Zhou H, Dong Q, Dai W, Cao H, Wang Z, Zeng H, Gong S, Gu G, Liang S, He M, Yang Z, Xu Q and Zhang Y** (2024) Overall transmission rate of 41.6 Gbit/s-0.22 THz OFDM upstream–downstream real-time transceivers facing over-500 m communication. *IEEE Transactions on Terahertz Science and Technology* **14**, 39–56.
7. **Boes F, T Messinger, J Antes, D Meier, A Tessmann, A Inam and I Kallfass** (2014) Ultra-broadband MMIC-based wireless link at 240 GHz enabled by 64GS/s DAC. In *39th International Conference on Infrared, Millimeter, and Terahertz waves (IRMMW-THz)*, 2014, IEEE, Tucson, AZ, USA. pp. 1–2.
8. **Nagatsuma T and K Maekawa** (2024) Single-carrier Over 200-Gbit/s and 200-m transmission in 300-GHz band. In *49th International Conference on Infrared, Millimeter, and Terahertz Waves (IRMMW-THz)*, 2024, IEEE, Perth, Australia. pp. 1–2.
9. **Hamada H, Tsutsumi T, Matsuzaki H, Fujimura T, Abdo I, Shirane A, Okada K, Itami G, Song H-J, Sugiyama H and Nosaka H** (2020) 300-GHz-band 120-Gb/s wireless front-end based on InP-HEMT PAs and mixers. *IEEE Journal of Solid-State Circuits* **55**, 2316–2335.
10. **Kürner T, Braun R-P, Ducournau G, Hellrung U, Hirata A, Hisatake S, John L, Jung BK, Kallfass I, Kawanishi T, Kondou K, Leiba Y, Napier B, Timar R, Renau A, Schlegel P, Szriftgiser P, Tessmann A and Wrana D** (2024) THz communications and the demonstration in the ThoR–Backhaul link. *IEEE Transactions on Terahertz Science and Technology* **14**, 554–567.
11. **Castro C, R Elschner, T Merkle, C Schubert and R Freund** (2020) Long-range high-speed thz-wireless transmission in the 300 GHz band. In *Third International Workshop on Mobile Terahertz Systems (IWMTS)*, 2020, IEEE, Essen, Germany. pp. 1–4.
12. **Dittmer J, J Tebart, C Füllner, C Koos, A Stöhr and S Randel** (2023) 200 Gbit/s wireless THz transmission over 52m using optoelectronic signal generation. In *53rd European Microwave Conference (EuMC)*, IEEE, Berlin, Germany. pp. 134–137.
13. **Takiguchi K** (2017) Real-time wireless OFDM communication in THz-band using optical dft processing. *International Topical Meeting on Microwave Photonics (MWP)*, IEEE, Beijing, China. pp. 1–3.
14. **Wu Y, C Han and T Yang** (2021) DFT-spread orthogonal time frequency space modulation design for terahertz communications. In *IEEE Global Communications Conference (GLOBECOM)*, 2021, IEEE, Madrid, Spain. pp. 01–06.
15. **Chen Y-W, Shen S, Zhou Q, Yao S, Zhang R, Omar S and Chang G-K** (2019) A reliable OFDM-Based MMW mobile fronthaul with DSP-Aided Sub-Band spreading and time-confined windowing. *Journal of Lightwave Technology* **37**, 3236–3243.
16. **Zhao Z, Vuran MC, Guo F and Scott SD** (2021) Deep-waveform: A learned OFDM receiver based on deep complex-valued convolutional networks. *IEEE Journal on Selected Areas in Communications* **39**, 2407–2420.
17. **Mashhadi MB and Gündüz D** (2021) Pruning the pilots: Deep learning-based pilot design and channel estimation for MIMO-OFDM systems. *IEEE Transactions on Wireless Communications* **20**, 6315–6328.
18. **Dörner S, Cammerer S, Hoydis J and t. Brink S** (2018) Deep learning based communication over the air. *IEEE Journal of Selected Topics in Signal Processing* **12**, 132–143.
19. **IEEE** (1999). *IEEE Standard for Telecommunications and Information Exchange between Systems – LAN/MAN Specific Requirements – Part 11: Wireless Medium Access Control (MAC) and Physical Layer (PHY) Specifications: High Speed Physical Layer in the 5 GHz Band*, IEEE Std 802. pp. 1–102.
20. **Tarboush S, Sarieddeen H, Alouini M-S and Al-Naffouri TY** (2022) Single- versus multicarrier terahertz-band communications: A comparative study. *IEEE Open Journal of the Communications Society* **3**, 1466–1486.
21. **Tubbax J, Van der Perre L, Engels M, De Man H and Moonen M** (2004) OFDM versus Single Carrier: A realistic multi-antenna comparison. *EURASIP Journal on Advances in Signal Processing* **320840** (2004), 1687–6180.

22. **Parisi CT, Badran S, Sen P, Petrov V and Jornet JM** (2024) Modulations for terahertz band communications: Joint analysis of phase noise impact and PAPR effects. *IEEE Open Journal of the Communications Society* **5**, 412–429.

23. **He D, Zhang Z, Lin H, Wu Z, Huang Y and Wang Z** (2024) Performance comparison of single-carrier and multi-carrier waveforms over terahertz wireless channels. *Digital Communications and Networks* **10**, 1297–1304, https://www.sciencedirect.com/science/article/pii/S2352864823001177

24. **Leuther A, A Tessmann, H Massler, R Losch, M Schlechtweg, M Mikulla and O Ambacher** (2008) 35 nm metamorphic HEMT MMIC technology. In *20th International Conference on Indium Phosphide and Related Materials*, 2008, IEEE, Versailles, France. pp. 1–4.

25. **Wrana D, John L, Schoch B, Wagner S and Kallfass I** (2022) Sensitivity analysis of a 280–312 GHz superheterodyne terahertz link targeting IEEE802.15.3d applications. *IEEE Transactions on Terahertz Science and Technology* **12**(4), 325–333.

26. **John L, A Tessmann, A Leuther, P Neininger, T Merkle and T Zwick** (2020) Broadband 300-GHz power amplifier MMICs in InGaAs mHEMT technology. *IEEE Transactions on Terahertz Science and Technology* **10**(3), 309–320.

27. **Zhang LM and Kschischang FR** (2014) Staircase codes with 6Overhead. *Journal of Lightwave Technology* **32**, 1999–2002.

28. **Shafik RA, MS Rahman and AR Islam** (2006) On the extended relationships among EVM, BER and SNR as performance metrics. In *International Conference on Electrical and Computer Engineering*, IEEE, Dhaka, Bangladesh. pp. 408–411.

29. **Kalpana N and Khan MZA** (2015) Fast computation of generalized water-filling problems. *IEEE Signal Processing Letters* **22**, 1884–1887.

30. **IEEE** (2020) *IEEE standard for low-rate wireless networks–Amendment 1: Enhanced Ultra Wideband (UWB) Physical Layers (PHYs) and Associated Ranging Techniques.* pp. 1–174.

31. **de Oliveira LG, D Brunner, A Diewald, C Muth, L Schmalen, T Zwick and B Nuss** (2023) Bistatic OFDM-based joint radar-communication: Synchronization, data communication and sensing. In *20th European Radar Conference (EuRAD)*, IEEE, Berlin, Germany. pp. 359–362.

32. **Patnaik A, Chaudhary N, Bhuyan MK, Alfarhood S and Safran M** (2024) Remote sensing single-image super-resolution using convolutional block attention residual network with joint adversarial mechanisms. *IEEE Access* **12**, 53424–53435.

Benjamin Schoch received his M.Sc. degree in power and microelectronics from Reutlingen University, Germany in 2016 in the frame of the Robert Bosch Center for Power Electronics. Since 2016, he has been a research and teaching assistant at the Institute of Robust Power Semiconductor Systems, University of Stuttgart, Germany in the area of millimeter and sub millimeterwave monolithic integrated circuits for broadband communication and radar imaging with a main research focus on power amplifier. Since 2022 he has taken over as the group leader of the millimeter wave department of the institute.

Dominik Wrana received the Master of Science degree in Electrical Engineering from Reutlingen University, Germany in 2019. Since 2019, he has been with the Institute of Robust Power Semiconductor Systems (ILH), University of Stuttgart, Germany as a research and teaching assistant. His current research focuses on the system- to circuit-level engineering for ultra-broadband wireless communications systems operating at millimeter and sub-millimeter wave frequencies. He is involved in the design and characterization of monolithic integrated circuits as well as system-level performance analysis and optimization.

Axel Tessmann received the Dipl.-Ing. degree in electrical engineering from the University of Karlsruhe, Germany, in 1997 and the Ph.D. degree in electrical engineering from the University of Karlsruhe, Germany, in 2006. In 1997, he joined the Microelectronics Department, Fraunhofer Institute for Applied Solid State Physics (IAF), Freiburg, Germany, where he is involved in the development of monolithically integrated circuits and subsystems for high-resolution imaging systems and high data rate wireless communication links. His main research areas are the design and packaging of millimeter-wave and submillimeter wave ICs as well as circuit simulation and linear and nonlinear device modeling. He is currently Group Manager of the millimeter wave packaging and subsystem group at the Fraunhofer IAF.

Ingmar Kallfass received the Dipl.-Ing. degree in Electrical Engineering from University of Stuttgart in 2000, and the Dr.-Ing. degree from University of Ulm in 2005 on the topic of nonlinear modelling of dispersive heterostructure field effect transistors and their MMIC applications. In 2001, he worked as a visiting researcher at the National University of Ireland, Dublin. In 2002, he joined the department of Electron Devices and Circuits of University of Ulm as a teaching and research assistant. In 2005, he joined the Fraunhofer Institute for Applied Solid-State Physics. From 2009 to 2012, he was a professor at the Karlsruhe Institute of Technology. Since 2013, he holds the chair for Robust Power Semiconductor Systems at the University of Stuttgart, where his major fields of research are compound semiconductor-based circuits and systems for power and microwave electronics. He is acting publications chair of the European Microwave Association (EuMA) and member of the Board of directors of the German Terhertz Center (DTZ) and the German Center for Satellite-Communications (DeSK). Together with his team, he forms a Competence Center of the European Center for Power Electronics (ECPE).

Simon Haussmann received his M.Sc. degree in power- and microelectronics at the Reutlingen University (Reutlingen, Germany) in 2018. After working in industry as an Electrical Engineer in research and development, he joined the University of Stuttgart at the Institute of Robust Power Semiconductor Systems in Stuttgart, Germany in 2021 as a researcher. His current research interests include THz-System Design, characterization and optimization of real-time mmW and sub-mmW communication systems.

Florian Euchner received the master's degree in electrical engineering and information technology from the University of Stuttgart, Germany, in 2021. Since then, he has been with the Institute of Telecommunications, University of Stuttgart. His research interests include channel charting and radio-based localization systems, raytracing for channel modeling, and practical synchronization aspects in distributed MIMO systems. As part of this work, he develops the channel sounder "DICHASUS" for data-driven massive MIMO research.